Acta Crystallographica Section A
Foundations of Crystallography
ISSN 0108-7673

Received 20 December 2003
Accepted 16 August 2004

Lattice imaging in low-angle and high-angle bright-field scanning transmission electron microscopy

K. Watanabe,[a] Y. Kikuchi,[b] T. Yamazaki,[c]* E. Asano,[c] N. Nakanishi,[c] Y. Kotaka,[d] E. Okunishi[e] and I. Hashimoto[c]

[a]Tokyo Metropolitan College of Technology, Tokyo, 140-0011 Japan, [b]Association of Super-Advanced Electronics Technologies (ASET), Kanagawa, 243-0198 Japan, [c]Department of Physics, Tokyo University of Science, Tokyo, 162-8601 Japan, [d]Materials & Material Engineering Laboratories, Fujitsu Laboratories Ltd, Kanagawa, 243-0197 Japan, and [e]JEOL Ltd, Tokyo, 196-8556 Japan. Correspondence e-mail: yamazaki@rs.kagu.tus.ac.jp

Atomic resolution low-angle bright-field (LABF) scanning transmission electron-microscope (STEM) images and high-angle bright-field (HABF) STEM images of [011]-orientated Si have been experimentally obtained together with high-angle annular dark-field (HAADF) STEM images. The contrast formation mechanisms of the LABF STEM and HABF STEM images are examined in comparison with HAADF STEM images. The HABF STEM images independent of defocus and thickness have spatial resolution comparable with HAADF STEM images, and are shown to be given as a simple convolution under the non-dispersion approximation of localized Bloch waves.

1. Introduction

High-resolution transmission electron microscopy (HRTEM) has been widely known as a tool for direct observation of an atomic structure in a nano area. However, the HRTEM images must be interpreted carefully because they do not always reveal the real atomic structure owing to the phase effect and lens aberration.

Scanning transmission electron microscopy (STEM) has an attractive feature that a variety of detector shapes and sizes is introduced to give different images. Various signals generated from the same specimen can be collected simultaneously and analyzed in parallel to get structural, compositional and electrical information. By using a low-angle annular dark-field (LAADF) STEM instrument, Crewe & Wall (1970) succeeded in detecting single atoms and atom clusters in the early 1970s. This imaging mode has, however, a disadvantage that the LAADF STEM images are controlled mainly by strong dynamical diffraction, so that the images depending on atomic number are obscured. By increasing the inner detector angle, the coherent Bragg scattering can be reduced and incoherent thermal diffuse scattering (TDS) increases (Howie, 1979). Pennycook & Jesson (1990) first proposed that the high-angle annular dark-field (HAADF) STEM with a large coherent convergent beam can provide incoherent atomic resolved images in a low-order zone axis. In the high-resolution HAADF STEM images, projected atomic columns are identified by bright spots independent of objective-lens defocus and sample thickness, unlike HRTEM images except for some objective-lens defocus conditions (Watanabe, Yamazaki, Kikuchi *et al.*, 2001). Furthermore, there are no Fresnel interference effects and the incoherent images give contrast depending strongly on atomic number (Mcgibbon *et al.*, 1995; Chisholm *et al.*, 1998; Yamazaki *et al.*, 2000; Voyles *et al.*, 2002). Extensive experimental and theoretical investigations lead to the contrast formation mechanism and the fundamental understanding of HAADF STEM images, such as effects of optical parameters of an instrument and small crystal tilt (Nellist & Pennycook, 1998; Pennycook & Nellist, 1999; Yamazaki *et al.*, 2002). To a good approximation, the HAADF STEM images are represented by a simple convolution between an intensity of an effective probe function and a compositionally sensitive object function (Pennycook & Jesson, 1991; Pennycook *et al.*, 2000). While this approximation is questionable for a thick specimen due to the spread of a localized wave along an atomic column, the clear projected atomic structure can be extracted for a relatively thin specimen from an obscure experimental image by the image processing based on the deconvolution (Watanabe *et al.*, 2002). The high efficiency of HAADF STEM images is amplified more by a recent development of a spherical aberration corrector for a probe forming system.

The atomic resolution images have also been obtained by bright-field (BF) STEM. Cowley (1969) suggested from the reciprocity theory that BF STEM imaging is identical to conventional transmission-electron-microscopy (CTEM) imaging when an on-axis point detector is used. It is demonstrated that a large collection angle of the BF detector gives a high-resolution image (Liu & Cowley, 1993) and its contrast has less dependence on the changes in objective-lens defocus and sample thickness (Xu *et al.*, 1990). However, the fundamental question associated with the contrast formation mechanism is not perfectly understood.

In this paper, we present experimental atomic resolved low-angle bright-field (LABF) STEM images and high-angle bright-field (HABF) STEM images of a [011]-orientated Si crystal together with HAADF STEM images. The contrast formation mechanisms of high-resolution LABF STEM and HABF STEM images are examined in comparison with HAADF STEM images with the aid of simulations, and the HABF STEM images are shown to be given as a simple convolution under the non-dispersion approximation of localized Bloch waves.

2. Experimental procedure

[011]-Si materials were prepared by mechanical polishing of a Czochralski-grown [100]-oriented *p*-type wafer. The cross-sectional specimens were prepared by a standard preparation technique including mechanical thinning, dimpling and subsequent Ar^+ ion milling. The ion millings were carefully carried out with a 3 keV ion beam at an incident angle as low as possible, followed by 1.7 keV ion milling so as to remove adhered amorphous and oxide surfaces. BF and HAADF STEM experiments were conducted using a JEM-2100F TEM/STEM operated at 200 keV, which has a probe forming lens of $C_s = 1.0$ mm. The semiangle of the incident probe α, the range of HAADF detector D, and the collection semiangles β of the BF detector were evaluated using microdiffraction, and were assigned to be $\alpha = 18$ mrad, $D = 70\sim240$ mrad, $\beta = 3$ and 18 mrad.

Image processing was performed by Fourier filtering, where a mask of 2.5 nm^{-1} diameter was used for each spot in a diffractogram of the image. Altering mask size, from 2 to 3 nm^{-1} does not have much of an effect on the final conclusion.

3. Image simulation

The dynamical simulations for both BF STEM and HAADF STEM images have already been discussed in detail by Watanabe, Yamazaki, Hashimoto & Shiojiri (2001), so this is only briefly outlined below. From the entrance and exit boundary conditions on crystal surfaces, the transmission coefficients $T_g(\mathbf{K}_\parallel, \mathbf{R}_0, t)$ at the sample thickness t are expressed for incident probe position vector $\mathbf{R}_0$ as

$$\begin{bmatrix} T_0(\mathbf{K}_\parallel, \mathbf{R}_0, t) \\ T_g(\mathbf{K}_\parallel, \mathbf{R}_0, t) \\ \vdots \end{bmatrix} = \exp(-i\mathbf{K}_\parallel \cdot \mathbf{R}_0) \exp(-iK_z t)\tilde{\mathbf{C}}(\mathbf{K}_\parallel) \cdot \tilde{\mathbf{G}}(\mathbf{K}_\parallel, t) \times \exp[-iW(\mathbf{K}_\parallel)]\tilde{\mathbf{C}}^{-1}(\mathbf{K}_\parallel) \cdot \bar{\mathbf{U}}, \quad (1)$$

where $\mathbf{K}_\parallel$ is the transverse component of the incident wavevector, K_z the longitudinal component of the wavevector in vacuum, $\bar{\mathbf{U}}$ a unit vector, matrix element $[\tilde{\mathbf{G}}(\mathbf{K}_\parallel, t)]_{i,j} = \exp[i\lambda^j(\mathbf{K}_\parallel)t]\delta_{i,j}$, and $\tilde{\mathbf{C}}(\mathbf{K}_\parallel)$ and $\tilde{\mathbf{C}}^{-1}(\mathbf{K}_\parallel)$, the matrix of eigenvectors and the inverse matrix, respectively. The complex eigenvalue $\lambda^j(\mathbf{K}_\parallel)$ is decomposed into its real part (the conventional '*Anpassung*' for branch j) and its imaginary part (the absorption for branch j).

3.1. Dynamical simulation for BF STEM images

The intensity of a BF STEM image formed by Bragg reflections, $I_{\rm BF}(\mathbf{R}_0, t)$, is defined by

$$I_{\rm BF}(\mathbf{R}_0, t) = \int D(\mathbf{K}_f)\left|\sum_g A(\mathbf{K}_f - \mathbf{g})T_g(\mathbf{K}_f - \mathbf{g}, \mathbf{R}_0, t)\right|^2 \mathrm{d}\mathbf{K}_f, \quad (2)$$

where $\mathbf{K}_f$ is the transverse component of the wavevector on the back focal plane, $A(\mathbf{K}_f - \mathbf{g})$ an objective-lens aperture function, and $D(\mathbf{K}_f)$ a detector function. The Fourier transform of equation (2) with respect to $\mathbf{R}_0$ is performed using spatial frequency $\mathbf{Q}$:

$$I_{\rm BF}(\mathbf{Q}, t) = \int \sum_g A(\mathbf{K}_\parallel)A^*(\mathbf{K}_\parallel + \mathbf{Q})D(\mathbf{K}_\parallel + \mathbf{g}) \times \exp\{i[W(\mathbf{K}_\parallel) - W(\mathbf{K}_\parallel + \mathbf{Q})]\} \times T'_g(\mathbf{K}_\parallel, t)T'^*_{g-Q}(\mathbf{K}_\parallel + \mathbf{Q}, t)\,\mathrm{d}\mathbf{K}_\parallel, \quad (3)$$

where $T'_g(\mathbf{K}_\parallel, t)\exp[iW(\mathbf{K}_\parallel)]\exp(-i\mathbf{K}_\parallel \cdot \mathbf{R}_0) = T_g(\mathbf{K}_\parallel, t)$ and $W(\mathbf{K}_\parallel)$ is a objective-lens aberration function. Equation (3) reveals some of the physics of the contrast formation mechanism. The intensity at a spatial frequency of $\mathbf{Q}$ arises from the interferences between partial incident and diffracted waves separated by $\mathbf{Q}$ and between $T'_g(\mathbf{K}_\parallel, t)$ and $T'^*_{g-Q}(\mathbf{K}_\parallel + \mathbf{Q}, t)$. Thus, even a small collection detector angle gives rise to high spatial resolution due to overlapping of convergent diffraction discs. Finally, the BF STEM image as a function of $\mathbf{R}_0$ is given by inverse Fourier transformation with respect to $\mathbf{Q}$:

$$I_{\rm BF}(\mathbf{R}_0, t) = \sum_Q I_{\rm BF}(\mathbf{Q}, t)\exp(-i\mathbf{Q} \cdot \mathbf{R}_0). \quad (4)$$

3.2. Dynamical simulation for HAADF STEM images

In HAADF STEM image calculations, our attention is focused on high-angle scattering of TDS among inelastic events. Thus, we used the two kinds of optical potential, $V'^{\rm all}_{g,\rm TDS}$ and $V'^{\rm ex}_{g,\rm TDS}$ (Watanabe, Yamazaki, Hashimoto & Shiojiri, 2001). The total optical potential, $V'^{\rm all}_g$, also includes atomic inner-shell ionization and plasmon loss. The total intensity of transmitted electrons, $I_{\rm all}(\mathbf{R}_0)$, can be calculated by using this total optical potential and removing the detector function from equation (3). Replacing $V'^{\rm all}_{g,\rm TDS}$ with $V'^{\rm ex}_{g,\rm TDS}$, we calculate $I_{\rm ex}(\mathbf{R}_0)$ where only electrons inelastically scattered outside the detector are considered as absorption. Then the total intensity $I^{\rm detector}_{\rm TDS}(\mathbf{R}_0)$ collected with the annular detector is simply calculated by $I^{\rm detector}_{\rm TDS}(\mathbf{R}_0) = I_{\rm ex}(\mathbf{R}_0) - I_{\rm all}(\mathbf{R}_0)$. In the present simulation of HAADF STEM images, we calculated just the contribution from TDS because the coherent scattering is negligible for images recorded with this detector angle.

The atomic scattering factors proposed by Weickenmeier & Kohl (1991) and the Debye–Waller factor of 0.0045 nm^2 were used (Rossouw *et al.*, 1994). The 000 component of core loss and plansmon loss was fixed to be 0.476 eV (Radi, 1970) and

the other components of core loss were neglected because the inelastic scattering processes are insignificant.

3.3. Convolution description for a BF STEM image

We shall find that it becomes particularly simple to answer the question whether HABF STEM images are described by a simple convolution by using a Bloch-wave description of the 1*s*-type bound state. This behavior is in marked contrast to CTEM imaging, in which all states at the exit surface contribute to the image, resulting in its strong thickness dependence. As mentioned above, the intensity of the coherent convergent beam at a relative thin specimen may be approximated by the non-dispersive 1*s*-type state contribution. To derive the convolution presentation for a HABF STEM image, the transmission coefficients in equation (3) are approximated by just the 1*s*-type state:

$$T_g(\mathbf{K}_\parallel, \mathbf{R}_0, t) = \exp(-i\mathbf{K}_\parallel \cdot \mathbf{R}_0)\alpha^{1s}(\mathbf{K}_\parallel)C_g^{1s}(\mathbf{K}_\parallel) \times \exp\{i[K_z + \gamma^{1s}(\mathbf{K}_\parallel)t]\}\exp\{-\mu^{1s}(\mathbf{K}_\parallel)t\}, \quad (5)$$

where $\alpha^{1s}(\mathbf{K}_\parallel)$ is the excitation amplitude of the 1*s*-type state, $C_g^{1s}(\mathbf{K}_\parallel)$ is the Bloch-wave amplitude for Bragg reflections, $\gamma^{1s}(\mathbf{K}_\parallel)$ is the *Anpassung* and $\mu^{1s}(\mathbf{K}_\parallel)$ is the absorption coefficient. Thus,

$$I_{\rm BF}(\mathbf{Q}, t) = \sum_g D_g \int A(\mathbf{K}_\parallel)A^*(\mathbf{K}_\parallel + \mathbf{Q})\exp\{i[W(\mathbf{K}_\parallel) - W(\mathbf{K}_\parallel + \mathbf{Q})]\} \times \alpha^{1s}(\mathbf{K}_\parallel)\alpha^{1s*}(\mathbf{K}_\parallel)C_g^{1s}(\mathbf{K}_\parallel)C_{g-Q}^{1s*}(\mathbf{K}_\parallel)\exp\{-2\mu^{1s}(\mathbf{K}_\parallel)t\}\,{\rm d}\mathbf{K}_\parallel. \quad (6)$$

The non-dispersion approximation means that the eigenvectors, the *Anpassung* and the absorption coefficient are independent of $\mathbf{K}_\parallel$ over the range of partial plane waves in the incident cone, thus resulting in

$$\begin{aligned} I_{\rm BF}(\mathbf{Q}, t) &= \sum_g D_g\alpha^{1s}(0)\alpha^{1s*}(0)C_g^{1s}(0)C_{g-Q}^{1s*}(0)\exp\{-2\mu^{1s}(0)t\} \\ &\quad \times \int \frac{\alpha^{1s}(\mathbf{K}_\parallel)\alpha^{1s*}(\mathbf{K}_\parallel)}{\alpha^{1s}(0)\alpha^{1s*}(0)}A(\mathbf{K}_\parallel)A^*(\mathbf{K}_\parallel + \mathbf{Q}) \\ &\quad \times \exp\{i[W(\mathbf{K}_\parallel) - W(\mathbf{K}_\parallel + \mathbf{Q})]\}\,{\rm d}\mathbf{K}_\parallel \\ &= o(\mathbf{Q}) \cdot p_{\rm eff}(\mathbf{Q}). \end{aligned} \quad (7)$$

When equation (7) is transformed back to real space, the product becomes the simple convolution between the object function $O(\mathbf{R}_0)$ and the effective probe intensity $P_{\rm eff}(\mathbf{R}_0)$:

$$I_{\rm BF}(\mathbf{R}_0) = O(\mathbf{R}_0) \otimes P_{\rm eff}(\mathbf{R}_0). \quad (8)$$

4. Results and discussion

4.1. Simulated results for LABF, HABF and HAADF STEM images

In order to discuss the effect of the collection angle of the BF detector, 3 and 18 mrad BF detectors are selected for LABF STEM and HABF STEM, respectively. Fig. 1 shows the relationship between the schematic [011] Si Kossel pattern and two BF detectors. The small collection angle covers only part of the 000 disc, while the large collection angle covers a wide area. Since the small collection angle may be regarded as a point BF detector, it might be expected that this imaging provides the image changes in defocus and thickness like high-resolution CTEM. A series of simulated through-focal and through-thickness BF STEM images is summarized in Fig. 2, where each Michelson visibility, V, is calculated so as to evaluate contrast quantitatively (Spence & Cowley, 1978). The LABF STEM provides a high-resolution image, but does not resolve dumbbells owing to the small information limit. The contrast shows the changes in defocus and thickness like HRTEM (Liu & Cowley, 1993). In particular, contrast reversal at atomic columns appears at sample thicknesses less than 20 nm. As the thickness increases, the images are less dependent on defocus, where an unresolved dumbbell corresponds to a dark spot. When the collection angle is very small, the intensity is mainly attributed to around $\mathbf{g} = (000)$ in equation (3). The contrast of the LABF STEM image is controlled by the spread of the localized wave formed by a coherent convergent beam at each probe position. The enhancement of a localized wave at each atomic column is,

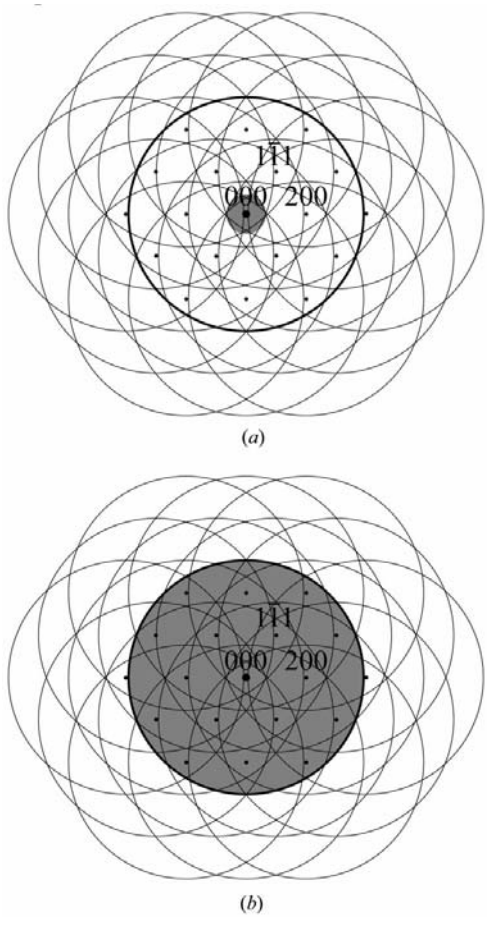

Figure 1
Outline of [011]-Si Kossel pattern and two collection semiangles of detector, $\beta = 3$ and 18 mrad. Large bold circles indicate the incident beam with semiangle 18 mrad.

however, insufficient at thin thickness. As a result, the difference in localized wave between the atomic columns and interatomic columns is largely affected by the defocus, leading to contrast reversal against defocus. At 40 nm thick, a large coherent convergent beam significantly makes the localized wave along an atomic column by the channeling (Fertig & Rose, 1981). Thus, atomic columns are identified by dark spots.

The calculations for through-focal and through-thickness HABF STEM images are shown in Fig. 3. All projected atomic positions are identified by dark spots and the images show no contrast reversal against thickness and defocus while details of black spots change with the defocus. Simulations based on the multislice method (Ishizuka, 2001) also demonstrated similar results. The spatial resolution becomes nearly equal to HAADF STEM although the resolution attainable in HAADF STEM is considered to be better by a factor of approximately 1.5 than the resolution obtainable in BF STEM using the same lens (Jesson *et al.*, 1991). A HABF STEM contrast depends on the total intensity of the diffraction plane because the 18 mrad BF detector almost covers the whole diffraction pattern, as shown in Fig. 1(*b*). When the incident convergent probe is located on the atomic column position, the channeling electrons are preferentially absorbed due to an enhancement of a localized wave compared with interatomic columns. The difference in absorption at respective positions of the incident convergent probe leads to the formation of HABF STEM images. As a result, HABF STEM images and HAADF STEM images are alike in the variations in objective-lens defocus and thickness exactly as expected for incoherent imaging. The enhancement of the wave along an atomic

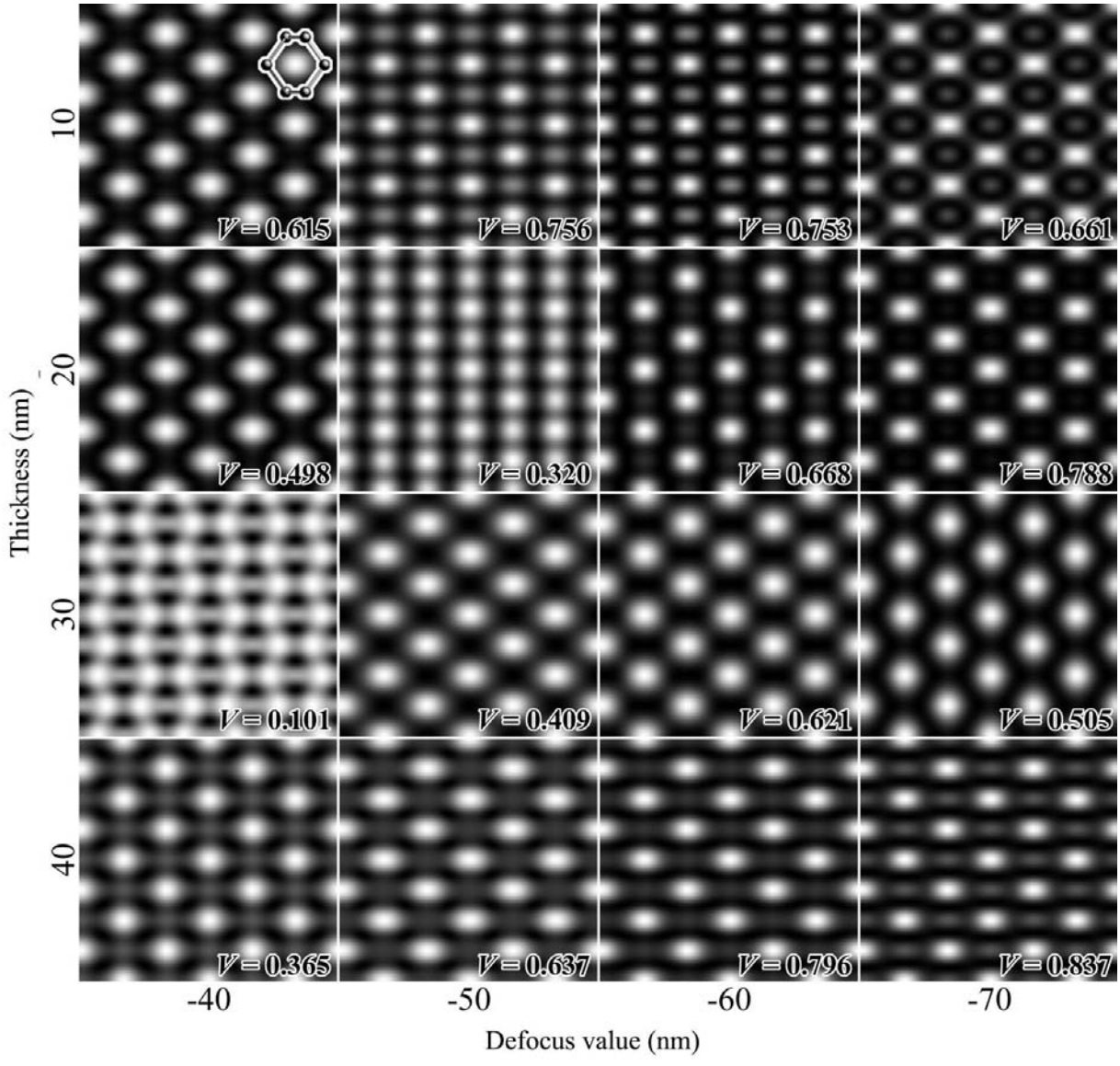

Figure 2
The simulated through-focal and through-thickness LABF STEM images at $\beta = 3$ mrad. The thickness and defocus values used for the simulation are indicated on the vertical and horizontal axes. In order to show the visibility of the respective images, the Michelson visibility, V, is indicated on each image. The projected atomic column positions are denoted by circles in the simulated image at $\Delta f = -40$ nm and $t = 10$ nm.

column and the absorption are critical factors in explaining the appearance of contrast in high-resolution HABF STEM.

4.2. Comparison between experimental and simulated images

Figs. 4(*a*) and (*b*) show high-resolution LABF STEM and HABF STEM images of a [011]-oriented Si crystal and a high-resolution HAADF STEM image is shown in Fig. 4(*c*). It is noted that the HABF STEM and HAADF STEM images were taken simultaneously. Figs. 4(*d*)–(*f*) and 4(*g*)–(*i*) show the corresponding Fourier diffractograms and Fourier filtering images, respectively. The Fourier filtering processing provides valuable images by decreasing the noise drastically as shown in Figs. 4(*g*)–(*i*). Reversed images are superimposed in each figure for ease of viewing. As shown in Figs. 4(*e*) and 4(*f*), where 113 components are high and 004 components are very small, the dumbbell spacing is slightly elongated (Watanabe *et al.*, 2003). There are slight differences in the same reflections due to sample drift, instability of instrument and small crystal tilt (Yamazaki *et al.*, 2002). The anisotropic tails interconnecting adjacent dumbbells may be mainly ascribed to these facts. BF STEM images are also very sensitive to the position of the BF detector because the area detecting the transmitted electrons at the diffraction plane is much smaller than the area for detecting electrons by the HAADF detector. Therefore, the slight deviation of the BF detector from the center of the 000 disc leads to a non-symmetric contrast (Yamazaki *et al.*, 2004). Furthermore, the S/N ratio of an experimental HABF STEM image is as small as that of a HAADF STEM image. It is thought that this is because the HABF STEM images are mainly formed by the absorption effect like HAADF STEM images.

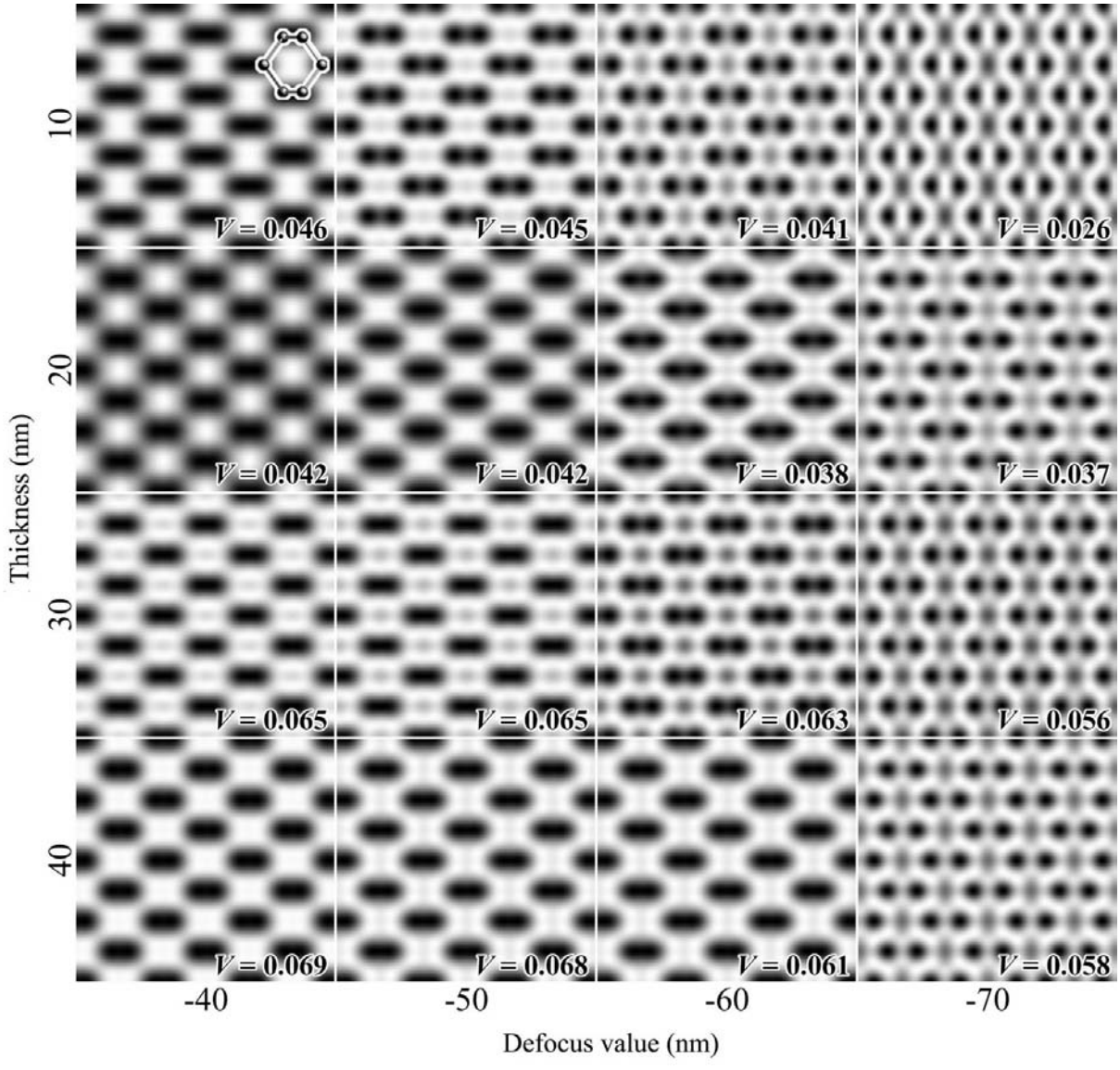

Figure 3
The simulated through-focal and through-thickness HABF STEM images at $\beta = 18$ mrad. The thickness and defocus values used for the simulation are indicated on the vertical and horizontal axes. In order to show the visibility of the respective images, the Michelson visibility, V, is indicated on each image. The projected atomic column positions are denoted by circles in the simulated image at $\Delta f = -40$ nm and $t = 10$ nm.

The HABF STEM produces clear resolved dumbbells, while the LABF STEM gives rise to unresolved spots in the dumbbell. From comparison with HAADF STEM images, HABF STEM can provide high spatial resolution comparable with HAADF STEM, able to be intuitively interpreted. Furthermore, observation of a HABF STEM image is easier than that of a HAADF STEM image. The corresponding calculated images are shown in Figs. 4(*j*)–(*l*). The simulations reproduce the corresponding experimental images satisfactorily, thereby confirming that our method can reproduce the observed BF STEM images well with the parameter values close to those used for the experimental observation.

4.3. Deconvolution processing for a HABF STEM image

As mentioned in §3.3, the HABF STEM image is described as a simple convolution between an object function and an effective probe function, so that the clear object function may be simply obtained from an obscure image by the deconvolution processing. While it is very difficult to determine the accurate defocus value experimentally, the defocus value may be determined by the maximum-entropy method (Watanabe *et al.*, 2002). In order to show the availability of the deconvolution processing combined with the maximum-entropy method, the raw experimental image and the processed version are exhibited in Figs. 5(*a*) and 5(*b*). The processed image reproduces clear resolved dumbbells, although a little anisotropic contrast remains. In spite of this anisotropic contrast, the deconvolution processing of HABF STEM images is valid for analyzing crystal structure like that of HAADF STEM images. A point to be noted is that an image obtained by this technique is not always the true projected structure because an experimental image used as material for deconvolution has information that is limited by the optical condition of the coherent convergent probe. In other words, the deconvolution leads to a projected structure image retrieved within the experimental information limit.

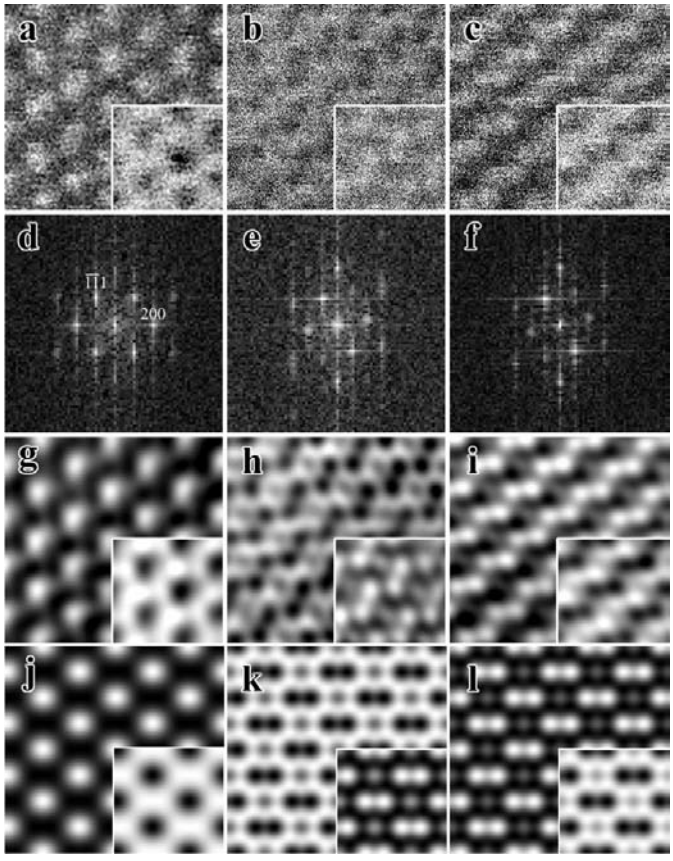

Figure 4
(*a*) The experimental raw LABF STEM image having unresolved dumbbell structure, (*b*) the experimental raw HABF STEM image having resolved dumbbell structure and (*c*) the experimental raw HAADF STEM image having resolved dumbbell structure. (*b*) and (*c*) are obtained simultaneously. (*d*)–(*f*) are Fourier diffractograms of the images of (*a*)–(*c*). (*g*)–(*i*) are noise-filtered images of (*a*)–(*c*), respectively. (*j*)–(*l*) are simulated LABF, HABF and HAADF STEM images of a [011]-orientated Si crystal 30 nm thick at $\Delta f = -60$ nm, respectively. Reversed images are superimposed in each figure.

5. Summary

High-resolution LABF STEM and HABF STEM images of [011]-orientated Si have been presented experimentally together with HAADF STEM images. The high-resolution LABF STEM images depend on sample thickness and objective-lens defocus like HRTEM. In contrast, the HABF STEM images are less dependent on sample thickness and defocus like HAADF STEM images, thus enabling us to intuitively determine projected atomic columns by black spots. Furthermore, the HABF STEM can provide high spatial resolution comparable with HAADF STEM and the HABF STEM image is presented by a simple convolution between an object function and an effective probe function. The deconvolution processing combined with the maximum-entropy method can be applied to retrieve a clear image from an obscure experimental HABF STEM image. The key to the contrast formation mechanism of LABF STEM is the enhancement of the localized wave formed along an atomic column, and that of HABF STEM images is both enhancement of the localized wave formed along an atomic column and absorption.

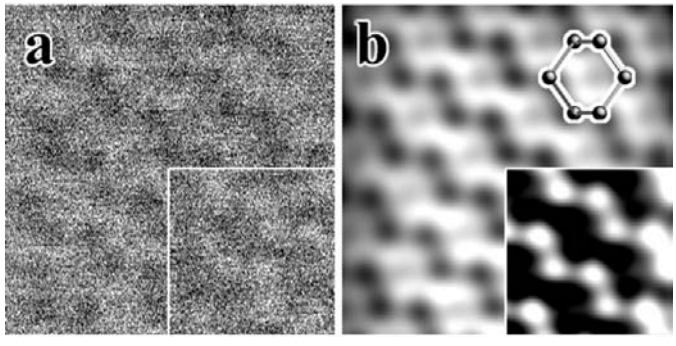

Figure 5
(*a*) An experimental image of [011]-orientated Si 30 nm thick. (*b*) Deconvoluted image of (*a*) using a probe function at $\Delta f = -62$ nm.

This research was partially supported by the Ministry of Education, Science, Sports and Culture, Grant-in-Aid for Scientific Research (C), 15560024, 2003. Two of the authors (TY and NN) are financially supported by the Japan Society for the Promotion of Science (JSPS) as JSPS Research Fellowships for Young Scientists.

References

Chisholm, M. F., Maiti, A., Pennycook, S. J. & Pantelides, S. T. (1998). *Phys. Rev. Lett.* **81**, 132–135.
Cowley, J. M. (1969). *Appl. Phys. Lett.* **15**, 58–59.
Crewe, A. V. & Wall, J. (1970). *Science*, **168**, 1338–1340.
Fertig, J. & Rose, H. (1981). *Optik (Stuttgart)*, **59**, 407–429.
Howie, A. (1979). *J. Microsc.* **117**, 11–23.
Ishizuka, K. (2001). *J. Electron Microsc.* **50**, 291–305.
Jesson, D. E., Pennycook, S. J. & Baribeau, J. M. (1991). *Phys. Rev. Lett.* **66**, 750–753.
Liu, J. & Cowley, J. M. (1993). *Ultramicroscopy*, **52**, 335–346.
Mcgibbon, A. J., Pennycook, S. J. & Angelo, J. E. (1995). *Science*, **269**, 518–521.
Nellist, P. D. & Pennycook, S. J. (1998). *Phys. Rev. Lett.* **81**, 4156–4159.
Pennycook, S. J. & Jesson, D. E. (1990). *Phys. Rev. Lett.* **64**, 938–941.
Pennycook, S. J. & Jesson, D. E. (1991). *Ultramicroscopy*, **37**, 14–38.
Pennycook, S. J. & Nellist, P. D. (1999). *Impact of Electron and Scanning Probe Microscopy on Material Reseach.* Dordrecht: Kluwer Academic Publishers.
Pennycook, S. J., Rafferty, B. & Nellist, P. D. (2000). *Microsc. Microanal.* **6**, 343–352.
Radi, G. (1970). *Acta Cryst.* A**26**, 41–56.
Rossouw, C. J., Spellward, P., Perovic, D. D. & Cherns, D. (1994). *Philos. Mag.* A**69**, 255–265.
Spence, J. C. H. & Cowley, J. M. (1978). *Optik (Stuttgart)*, **50**, 129–142.
Voyles, P. M., Muller, D. A., Grazul, J. L., Citrin, P. H. & Gossmann, H. J. L. (2002). *Nature (London)*, **416**, 826–829.
Watanabe, K., Kotaka, Y., Nakanishi, N., Yamazaki, T., Hashimoto, I. & Shiojiri, M. (2002). *Ultramicroscopy*, **92**, 191–199.
Watanabe, K., Nakanishi, N., Yamazaki, T., Kawasaki, M., Hashimoto, I. & Shiojiri, M. (2003). *Phys. Status Solidi B*, **235**, 179.
Watanabe, K., Yamazaki, T., Hashimoto, I. & Shiojiri, M. (2001). *Phys. Rev. B*, **64**, 115432(1)–115432(5).
Watanabe, K., Yamazaki, T., Kikuchi, Y., Kotaka, Y., Kawasaki, M., Hashimoto, I. & Shiojiri, M. (2001). *Phys. Rev. B*, **63**, 085316(1)–085316(5).
Weickenmeier, A. & Kohl, H. (1991). *Acta Cryst.* A**47**, 590–597.
Xu, P., Kirkland, E. J. & Silcox, J. (1990). *Ultramicroscopy*, **32**, 93–102.
Yamazaki, T., Kawasaki, M., Watanabe, K., Hashimoto, I. & Shiojiri, M. (2002). *Ultramicroscopy*, **92**, 181–189.
Yamazaki, T., Kikuchi, Y., Watanabe, K., Nakanishi, N., Asano, E., Okunishi, E. & Hashimoto, I. (2004). *Proceedings of 13th European Microscopy Congress*. In the press.
Yamazaki, T., Watanabe, K., Kikuchi, Y., Kawasaki, M., Hashimoto, I. & Shiojiri, M. (2000). *Phys. Rev. B*, **61**, 13833–13839.